Design and Experimental Implementation of a Compliant Hybrid Zero Dynamics Controller with Active Force Control for Running on MABEL

Koushil Sreenath, Hae-Won Park, J. W. Grizzle

***Abstract*— This paper presents a control design based on the method of virtual constraints and hybrid zero dynamics to achieve stable running on MABEL, a planar biped with compliance. In particular, a time-invariant feedback controller is designed such that the closed-loop system not only respects the natural compliance of the open-loop system, but also enables active force control within the compliant hybrid zero dynamics and results in exponentially stable running gaits. The compliant-hybrid-zero-dynamics-based controller with active force control is implemented experimentally and shown to realize stable running gaits on MABEL at an average speed of 1.95 m/s (4.4 mph) and a peak speed of 3.06 m/s (6.8 mph). The obtained gait has flight phases upto 39% of the gait, and an estimated ground clearance of $7.5 - 10$ cm.**

I. Introduction

Running is an extremely agile motion, typically characterized by the presence of a flight phase with the feet off the ground. Early dynamically stable running robots employed the natural dynamics of the system through simple intuitive controllers, proposed by Raibert [13], to achieve life-like running gaits. Hopping on a planar monopod at speeds upto 5.9 m/s was demonstrated [6]. The use of Raibert's controllers to achieve stable running is typically possible on robots with favorable natural dynamics and appropriate morphology.

On bipedal robots that are not specifically designed mechanically for running, the ZMP criterion has been employed to demonstrate running gaits. See results on running on Sony's QRIO [9], Honda's ASIMO, Toyota's humanoid robot [17] (with running at a top speed of 1.94 m/s), HRP-2LR [5], HRP-2LT [4], and HUBO [1]. In these robots, some form of ZMP regulation is used during the stance phase to prevent the foot from rolling. The obtained running gaits have short flight times and low ground clearance during flight.

Around the same time, running was excited on RABBIT, with a significant flight duration and good ground clearance, through a controller based on the hybrid zero dynamics framework [8]. However, the running was not sustained. A few reasons for this technical failure were: (a) the actuators were forced to behave like a spring, performing negative work on impact to redirect the COM upwards, requiring 95% of the maximum torque of the motors for the nomial gait, leaving very little torque for feedback correction; (b) the controller resulted in bad ground contact forces during transients [12]. This led to the design of MABEL, a planar biped, which incorporated compliance in the transmission for shock absorption and for storing and releasing the impact energy for the purpose of energy efficiency. The robot weighs 65 kg, has 1 m long legs, and is mounted on a boom of radius 2.25 m. Figure 1 briefly illustrates the transmission of MABEL; for further details on the mechanical design, see [3].

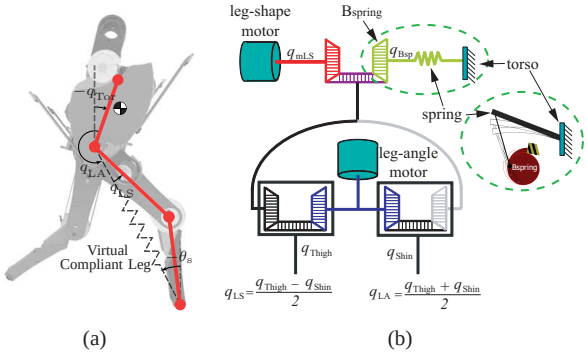

Fig. 1. (a) The *virtual compliant leg* created by the drivetrain through a set of differentials. The coordinate system used for the linkage is also indicated. Angles are positive in the counter clockwise direction. (b) MABEL's drivetrain (same for each leg), all housed in the torso. Two motors and a spring are connected to the traditional hip and knee joints via three differentials. On the robot, the differentials are realized via cables and pulleys [3] and not via gears. They are connected such that the actuated variables are leg angle and leg shape, so that the spring is in series with the leg-shape motor. The base of the spring is grounded to the torso and the other end is connected to the $\mathrm{B}_{\mathrm{spring}}$ differential via a cable, which makes the spring *unilateral*. When the spring reaches its rest length, the pulley hits a hard stop, formed by a very stiff damper. When this happens, the leg-shape motor is, for all intents and purposes, rigidly connected to leg shape through a gear ratio.

The remainder of the paper is organized as follows. Section II presents a mathematical model for MABEL, Section III presents the technical details for the control design, Section IV presents an experimental validation of the running controller, and Section V presents concluding remarks.

II. MABEL's Model

A. MABEL's Unconstrained Dynamics

The configuration space Q_{e} of the unconstrained dynamics of MABEL is an open simply-connected subset of $\mathbb{S}^7 \times \mathbb{R}^2$: five DOF are associated with the links in the robot's body, two DOF are associated with the springs in series with the two leg-shape motors, and two DOF are associated with the

Koushil Sreenath and J. W. Grizzle are with the Control Systems Laboratory, Electrical Engineering and Computer Science Department, University of Michigan, Ann Arbor, MI 48109-2122, USA. {koushils, grizzle}@umich.edu

Hae-Won. Park is with the Mechanical Engineering Department, University of Michigan, Ann Arbor, MI 48109-2125, USA. parkhw@umich.edu

This work is supported in part by NSF grant ECS-909300 and in part by DARPA Contract W91CRB-11-1-0002. An extended version of this paper with several other experiments and results has been submitted [15].

horizontal and vertical position of the robot in the sagittal plane. A set of coordinates suitable for parametrization of the robot's linkage and transmission is, $q_{\mathrm{e}} := (\ q_{\mathrm{LA_{st}}};\ q_{\mathrm{mLS_{st}}};\ q_{\mathrm{Bsp_{st}}};\ q_{\mathrm{LA_{sw}}};\ q_{\mathrm{mLS_{sw}}};\ q_{\mathrm{Bsp_{sw}}};\ q_{\mathrm{Tor}};\ p^h_{\mathrm{hip}};\ p^v_{\mathrm{hip}}\ )$, where, as in Figure 1, q_{Tor} is the torso angle, and $q_{\mathrm{LA_{st}}}$, $q_{\mathrm{mLS_{st}}}$, and $q_{\mathrm{Bsp_{st}}}$ are the leg angle, leg-shape motor position and $\mathrm{B_{spring}}$ position respectively for the stance leg. The swing leg variables, $q_{\mathrm{LA_{sw}}}$, $q_{\mathrm{mLS_{sw}}}$ and $q_{\mathrm{Bsp_{sw}}}$ are defined similarly. For each leg, q_{LS} is uniquely determined by a linear combination of q_{mLS} and q_{Bsp}, reflecting the fact that the cable differentials place the spring in series with the motor, with the pulleys introducing a gear ratio. The coordinates $p^h_{\mathrm{hip}}, p^v_{\mathrm{hip}}$ are the horizontal and vertical positions of the hip in the sagittal plane.

The equations of motion are obtained using the method of Lagrange. In computing the Lagrangian, the total kinetic energy is taken to be the sum of the kinetic energies of the transmission, the rigid linkage, and the boom. The potential energy is computed in a similar manner with the difference being that the transmission contributes to the potential energy of the system only through its non-elastic energy (the mass). This distinction is made since it is more convenient to model the unilateral spring as an external input to the system. The resulting model of the robot's unconstrained dynamics is determined as

$$D_{\mathrm{e}}\left(q_{\mathrm{e}}\right)\ddot{q}_{\mathrm{e}} + C_{\mathrm{e}}\left(q_{\mathrm{e}}, \dot{q}_{\mathrm{e}}\right)\dot{q}_{\mathrm{e}} + G_{\mathrm{e}}\left(q_{\mathrm{e}}\right) = \Gamma_{\mathrm{e}}, \tag{1}$$

where, D_{e} is the inertia matrix, C_{e} contains Coriolis and centrifugal terms, G_{e} is the gravity vector, and Γ_{e} is the vector of generalized forces acting on the robot, expressed as,

$$\begin{aligned}\Gamma_{\mathrm{e}} = {} & B_{\mathrm{e}}u + E_{\mathrm{ext}}\left(q_{\mathrm{e}}\right)F_{\mathrm{ext}} + \\ & B_{fric}\tau_{fric}\left(q_{\mathrm{e}}, \dot{q}_{\mathrm{e}}\right) + B_{sp}\tau_{sp}\left(q_{\mathrm{e}}, \dot{q}_{\mathrm{e}}\right),\end{aligned} \tag{2}$$

where the matrices B_{e}, E_{ext}, B_{fric}, and B_{sp} are derived from the principle of virtual work and define how the actuator torques u, the external forces F_{ext} at the leg, the joint friction forces τ_{fric}, and the spring torques τ_{sp} enter the model respectively. The dimension of u is four, corresponding to the two brushless DC motors on each leg for actuating leg shape and leg angle.

B. MABEL's Constrained Dynamics

The model (1) can be particularized to describe the stance and flight dynamics by incorporating proper holonomic constraints.

1) Dynamics of Stance: For modeling the stance phase, the stance toe is assumed to act as a passive pivot joint (no slip, no rebound and no actuation). Hence, the Cartesian position of the hip, $\left(p^h_{\mathrm{hip}}, p^v_{\mathrm{hip}}\right)$, is defined by the coordinates of the stance leg and torso. The springs in the transmission are appropriately chosen to support the entire weight of the robot, and hence are stiff. Consequently, it is assumed that the spring on the swing leg does not deflect, that is, $q_{\mathrm{Bsp_{sw}}} \equiv 0$. The stance configuration space, Q_{s}, is therefore a co-dimension three submanifold of Q_{e}. With these assumptions, the generalized configuration variables in stance are taken as $q_{\mathrm{s}} := \left(q_{\mathrm{LA_{st}}}; q_{\mathrm{mLS_{st}}}; q_{\mathrm{Bsp_{st}}}; q_{\mathrm{LA_{sw}}}; q_{\mathrm{mLS_{sw}}}; q_{\mathrm{Tor}}\right)$. Defining the state vector $x_{\mathrm{s}} := (q_{\mathrm{s}}; \dot{q}_{\mathrm{s}}) \in TQ_{\mathrm{s}}$, the stance dynamics can be expressed in standard form as,

$$\dot{x}_{\mathrm{s}} = f_{\mathrm{s}}(x_{\mathrm{s}}) + g_{\mathrm{s}}(x_{\mathrm{s}})u. \tag{3}$$

2) Dynamics of Flight: In the flight phase, both feet are off the ground, and the robot follows a ballistic motion under the influence of gravity. Thus the flight dynamics can be modeled by the unconstrained dynamics developed earlier. However an additional assumption can be made to eliminate the stiffness in integrating the differential equations representing the flight model. As mentioned, the springs must be stiff to support the entire weight of the robot. Further, since neither leg is in contact with the ground during the flight phase, it can be assumed that the springs on each leg do not deflect during the flight phase[1]. Therefore, $q_{\mathrm{Bsp_{st}}} \equiv 0, q_{\mathrm{Bsp_{sw}}} \equiv 0$. Thus, the configuration space of the flight dynamics is a co-dimension two submanifold of Q_{e}, i.e., $Q_{\mathrm{f}} := \left\{q_{\mathrm{e}} \in Q_{\mathrm{e}} \mid q_{\mathrm{Bsp_{st}}} \equiv 0, q_{\mathrm{Bsp_{sw}}} \equiv 0\right\}$. It follows that the generalized configuration variables in the flight phase can be taken as $q_{\mathrm{f}} := \left(q_{\mathrm{LA_{st}}}; q_{\mathrm{mLS_{st}}}; q_{\mathrm{LA_{sw}}}; q_{\mathrm{mLS_{sw}}}; q_{\mathrm{Tor}}; p^h_{\mathrm{hip}}; p^v_{\mathrm{hip}}\right)$. Defining the state vector $x_{\mathrm{f}} := (q_{\mathrm{f}}; \dot{q}_{\mathrm{f}}) \in TQ_{\mathrm{f}}$, the flight dynamics can be expressed in standard form as,

$$\dot{x}_{\mathrm{f}} = f_{\mathrm{f}}(x_{\mathrm{f}}) + g_{\mathrm{f}}(x_{\mathrm{f}})u. \tag{4}$$

C. MABEL's Transitions

1) Stance to Flight Transition Map: Physically, the robot takes off when the normal component of the ground reaction force acting on the stance toe, $F^N_{toe_{\mathrm{st}}}$, becomes zero. The ground reaction force at the stance toe can be computed as a function of the acceleration of the COM and thus depends on the inputs $u \in \mathcal{U}$ of the system described by (3). Mathematically, the transition occurs when the solution of (3) intersects the co-dimension one switching manifold

$$\mathcal{S}_{\mathrm{s}\to\mathrm{f}} := \left\{x_{\mathrm{s}} \in TQ_{\mathrm{s}} \times \mathcal{U} \mid F^N_{toe_{\mathrm{st}}} = 0\right\}. \tag{5}$$

On transition from the stance to flight phase, the stance leg comes off the ground and takeoff occurs. During the stance phase, the spring on the stance leg is compressed. When the stance leg comes off the ground, the spring rapidly decompresses and impacts the hard stop. The stance to flight transition map, $\Delta_{\mathrm{s}\to\mathrm{f}} : \mathcal{S}_{\mathrm{s}\to\mathrm{f}} \to TQ_{\mathrm{f}}$ accounts for this. Further details are omitted for the sake of brevity and interested readers are referred to [15].

2) Flight to Stance Transition Map: The robot physically transitions from flight phase to stance phase when the swing toe contacts the ground surface. The impact is modeled here as an inelastic contact between two rigid bodies. It is assumed that there is no rebound or slip at impact. Mathematically, the transition occurs when the solution of (4) intersects the co-dimension one switching manifold

$$\mathcal{S}_{\mathrm{f}\to\mathrm{s}} := \left\{x_{\mathrm{f}} \in TQ_{\mathrm{f}} \mid p^v_{\mathrm{toe_{sw}}} = 0\right\}. \tag{6}$$

[1]The pre-tension in the cables between the spring and the pulley $\mathrm{B_{spring}}$ (see Figure 1b) has been set as close to zero as possible to ensure the spring is not pre-loaded.

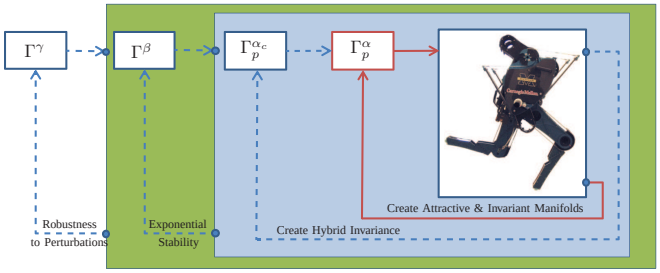

Fig. 2. Feedback diagram illustrating the running controller structure. Continuous lines represent signals in continuous time; dashed lines represent signals in discrete time. The controllers Γ_p^{α} and $\Gamma_p^{\alpha_c}$ create a compliant actuated hybrid zero dynamics. The controller Γ^{β} ensures that the periodic orbit on the resulting zero dynamics manifold is locally exponentially stable. The controller Γ^{γ} increases the robustness to perturbations in the knee angle at impact and to imperfections in the ground contact model.

In addition to modeling the impact of the leg with the ground, and the associated discontinuity in the generalized velocities of the robot [2], the transition map accounts for the assumption that the spring on the new swing leg remains at its rest length, and for the relabeling of the robot's coordinates so that only one stance model is necessary. In particular, the transition map $\Delta_{\mathrm{f}\to\mathrm{s}} : \mathcal{S}_{\mathrm{f}\to\mathrm{s}} \to TQ_{\mathrm{s}}$ consists of three subphases executed in the following order: (a) standard rigid impact model [2]; (b) adjustment of spring velocity in the new swing leg; and (c) coordinate relabeling.

D. Hybrid model of Running

The hybrid model of running is based on the dynamics developed in Section II-B and the transition maps presented in Section II-C, and is given by

$$\Sigma_{\mathrm{s}} : \begin{cases} \dot{x}_{\mathrm{s}} = f_{\mathrm{s}}(x_{\mathrm{s}}) + g_{\mathrm{s}}(x_{\mathrm{s}})\,u, & (x_{\mathrm{s}}^-, u^-) \notin S_{\mathrm{s}\to\mathrm{f}} \\ x_{\mathrm{f}}^+ = \Delta_{\mathrm{s}\to\mathrm{f}}(x_{\mathrm{s}}^-, u^-), & (x_{\mathrm{s}}^-, u^-) \in S_{\mathrm{s}\to\mathrm{f}} \end{cases}$$

$$\Sigma_{\mathrm{f}} : \begin{cases} \dot{x}_{\mathrm{f}} = f_{\mathrm{f}}(x_{\mathrm{f}}) + g_{\mathrm{f}}(x_{\mathrm{f}})\,u, & x_{\mathrm{f}}^- \notin S_{\mathrm{f}\to\mathrm{s}} \\ x_{\mathrm{s}}^+ = \Delta_{\mathrm{f}\to\mathrm{s}}(x_{\mathrm{f}}^-), & x_{\mathrm{f}}^- \in S_{\mathrm{f}\to\mathrm{s}}. \end{cases} \tag{7}$$

III. Control Design for Running

This section presents a controller design for inducing stable running motions on MABEL. The controller will create an actuated compliant HZD enabling active force control within the HZD.

Virtual constraints for the stance phase of running are chosen in a manner similar to that of walking [16] such that the open-loop compliance of the system is preserved as a dominant characteristic of the closed-loop system. However, by implementing one less virtual constraint in the stance phase than the maximum possible, an actuator is left free and will result in the zero dynamics being actuated. Through this actuator, active force control will be introduced as a means of varying the effective compliance of the system.

A. Virtual Constraint Design and Active Force Control

Virtual constraints [18] are holonomic constraints that are parametrized by a monotonic function of the state and imposed through feedback control, with the purpose being to restrict the dynamics to evolve on lower-dimensional surfaces embedded in the state spaces of the stance and flight dynamics. This lower-dimensional hybrid system governs the existence and the stability of periodic solutions corresponding to running motions. The virtual constraints for running can be described by a choice of outputs,

$$y_p = H_0^p q_p - h_d^p(\theta_p(x_p), \alpha_p, \alpha_c^p, \beta, \gamma), \tag{8}$$

where $p \in \mathcal{P} = s, f$, and h_d^p is the desired evolution of the virtual constraints which is parametrized by Bézier polynomials with coefficients α_p. The other Bézier polynomial coefficients, α_c^p, β, and γ are zero for the nominal gait and are updated in an event-based manner. In particular, α_c^p parametrize correction polynomials that are used to create hybrid invariance, while β and γ are used by outer-loop event-based controllers to make step-to-step updates to the virtual constraints as will be seen in Section III-C.

For the stance phase, H_0^{s} is based on the walking controller introduced in [16], but with the stance leg-shape motor variable omitted. A virtual constraint on the the torso position provides a desired profile for the torso, and two virtual constraints on the swing leg angle and the swing leg-shape motor describe the evolution of the swing leg. With the choice of these three virtual constraints, the stance zero dynamics is both compliant and actuated, see [15]. The stance virtual constraints are parametrized as a function of θ_{s}, shown in Figure 1a.

The stance leg-shape motor is the actuator that moves into the zero dynamics. Due to the transmission in MABEL, this actuator is in series with the spring. By imposing a torque of the form $u_{\mathrm{mLS_{st}}} = -k_{\mathrm{vc}}(q_{\mathrm{mLS_{st}}} - q_{\mathrm{mLS_{vc}}})$ on this actuator, a virtual compliant element with stiffness k_{vc} and rest position $q_{\mathrm{mLS_{vc}}}$ is created and placed in series with the physical compliance. This active force control strategy enables changing the effective compliance of the stance leg dynamically. However, to keep the controller simple, the virtual-compliance parameters are modified only once during the stance phase. The stance phase is artificially divided into stance-compression (sc) and stance-decompression (sd) subphases, and the parameters for the virtual compliance are updated only at this transition.

For the flight phase, H_0^{f} is chosen as follows. On the stance leg[2], the leg angle and leg-shape motor variables are chosen, and on the swing leg, the absolute leg angle and leg-shape motor variables are chosen. The absolute leg angle on the swing leg enables directly specifying the touchdown angle through a virtual constraint. The flight virtual constraints are parametrized as a function of θ_{f}, which is chosen as the horizontal position of the hip, as in RABBIT [8].

The choice of the desired evolution of the virtual constraints, h_d^p for the stance and flight phases, and the choice of the virtual compliance for the stance-compression and stance-decompression subphases are left as free parameters to be found by optimization.

[2]The stance leg in the flight phase refers to the leg that was on the ground prior to the flight phase.

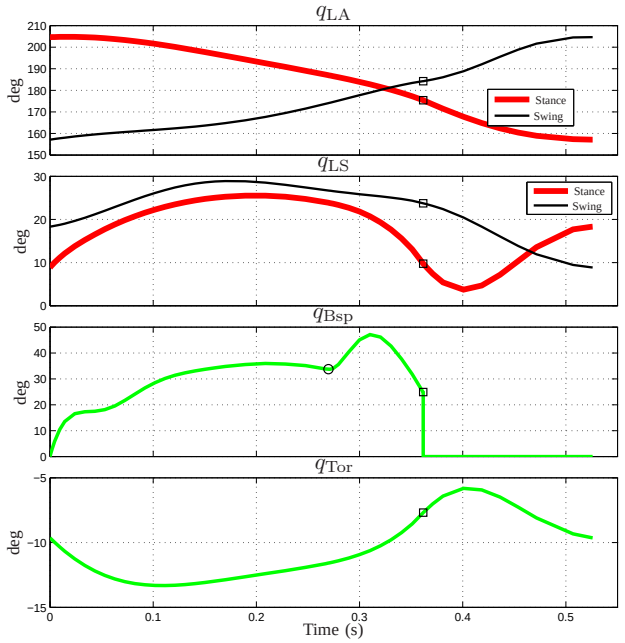

Fig. 3. Evolution of the virtual constraints and configuration variables for a nominal fixed point (periodic running gait) at a speed of 1.34 m/s and step length 0.7055 m. The squares illustrate the location of transition between stance to flight phase.

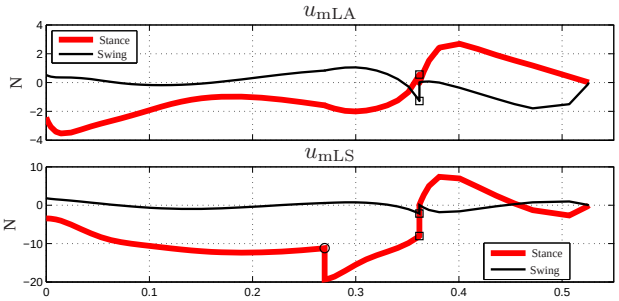

Fig. 4. Actuator torques corresponding to the nominal fixed point. The squares illustrate the location of transition between stance to flight phase. The circle on the $u\mathrm{mLS}_{\mathrm{st}}$ plot illustrates the location of the *sc* to *sd* event transition. Note that the torques are discontinuous at stance to flight transitions. Also note the additional discontinuity for $u\mathrm{mLS}_{\mathrm{st}}$ at the *sc* to *sd* event transition due to the instantaneous change in the offset for the virtual compliance at this transition.

B. Fixed Point for Running

A periodic running gait is designed by selecting the free parameters in the virtual constraints and the virtual compliance through constrained numerical optimization of the nominal model (see [18, Ch. 6]). A nominal fixed point representing running at 1.34 m/s was obtained with a step time of 525 ms, with 69% spent in stance and 31% in flight. Figures 3-4 illustrate various variables for the nominal fixed point. In all of these figures, the squares on the plots indicate the location of the transition from stance to flight phase.

Figure 3 illustrates the nominal evolution of the virtual constraints and configuration variables for the stance and flight phases for one step of running. The circle in the spring plot indicates the location of stance-compression to stance-decompression transition. During the stance-compression phase, the spring compresses, reaches its peak value of almost $36°$, and starts to decompress. On transition to the stance-decompression phase, a change in the virtual compliance parameters causes the motor to inject energy into the system, causing the spring to rapidly compress to a peak of $47°$. At lift-off, when the vertical component of the ground force goes to zero, the spring has decompressed to approximately $25°$. On transition to flight, the spring is reset to its rest position by an instantaneous change in the leg-shape motor position. During the flight phase, the stance leg shape initially unfolds due to the large velocity of push-off during the final part of the stance phase as the spring rapidly decompresses.

Figure 4 illustrates the actuator torques used to realize the gait. The stance and swing leg-angle torque and the swing leg-shape torque are small compared to the peak torque capacities of the actuators: 30Nm. The stance leg-shape torque is large, initially to support the weight of the robot as the stance knee bends and subsequently to provide sufficient energy injection in the stance-decompression phase to achieve lift-off. The stance leg-shape motor torque is discontinuous at the stance-compression to stance-decompression transition due to an instantaneous change in the parameters for the virtual compliance. All torques are discontinuous on the stance to flight transition due to the impact of the spring with the hard-stop.

C. Closed-loop Design and Stability Analysis

The periodic running motion in the previous section was found by studying the restricted hybrid dynamics of the system. We now need to design a controller that creates the lower-dimensional surfaces and makes them invariant and attractive. In the following, we introduce control action on three levels with an inner-loop and two outer-loops. On the first level, a continuous-time controller is presented that in addition to rendering the zero dynamics invariant also makes it attractive. The hybrid invariance is still achieved through the correction polynomials on a event to event level [7]. On the second level, an outer-loop event-based discrete linear controller is introduced to exponentially stabilize the periodic orbit representing the running gait. Finally on the third level, an additional outer-loop event-based nonlinear controller is introduced to increase the robustness to perturbations in the knee angle at impact and to imperfections in the ground contact model; see Figure 2.

The classic input-output linearizing controller [18, Ch. 5] is used as Γ_p^α to render the zero dynamics both invariant and attractive. The correction polynomials create hybrid invariance and are updated step-to-step by $\Gamma_p^{\alpha_c}$. The stability of the fixed point under the above controller can be studied by the method of Poincaré. We consider the stance-compression to stance-decompression switching surface, $\mathcal{S}_{sc\to sd}$, as a Poincaré section, and define the Poincaré map $P : \mathcal{S}_{sc\to sd} \to \mathcal{S}_{sc\to sd}$. Using this Poincaré map, we can numerically calculate the eigenvalues of its linearization about the fixed point. Numerical analysis shows that the obtained running gait has

a dominant eigenvalue of 1.1928 and is unstable. Thus, an additional controller needs to be designed to stabilize the running fixed point.

An outer-loop discrete event-based linear controller can be designed to stabilize the discrete linear system representing the linearized Poincaré map, as was done for Thumper in [11]. We identify certain parameters that can be varied step-to-step, and which could possibly affect stability of the fixed point. We choose the following parameters to be varied step-to-step: the stiffness and rest position parameters for the virtual compliance for the stance-compression and stance-decompression subphases, the touchdown angle, the torso offset and finally a parameter to change the flight duration. The linearized Poincaré map is obtained numerically and discrete LQR is used to find a feedback, Γ^{β}, that stabilizes the fixed point of the Poincaré map. On carrying out this procedure, we obtain a dominant eigenvalue of 0.8383, which shows that the fixed point is locally exponentially stabilized with this controller.

Next, prior to experimental validation, we study the robustness of the controller to perturbations. Perturbations in torso angle at impact are studied since tracking errors for the heavy torso (40 kg) could potentially influence the dynamics of running significantly. This controller can reject an error in torso of up to 6° in both directions, which is fairly good robustness to perturbations in torso angle. However, the controller is unable to reject an error in the form of the stance leg shape being bent by an additional 5°. Thus, there is a need for a controller that can improve the robustness to perturbations in the knee angle at impact. This will be crucial for experimental validation.

The outer-loop Γ^{γ} controller is a heuristic nonlinear controller based on insight into simple models. For instance, on landing on a bent knee, the virtual compliance can be stiffened to prevent the stance leg from collapsing, thereby improving robustness to perturbations in the impact value of the stance leg shape. This outer-most controller is highly dependent on the morphology of the system and exists only to improve the robustness to perturbations in an experimental setting. The stability of the fixed point under the action of Γ^{γ} can once again be studied by the method of Poincaré by sampling the closed-loop hybrid system with the outer-loop Γ^{β} controller on a suitable Poincaré Section. Performing this numerically, a dominant eigenvalue of 0.6072 is obtained ensuring that the closed-loop system is stable.

IV. Experimental Validation of the Running Controller

The running controller of Section III created stable running motions. This section documents experimental implementation of this controller on MABEL.

Before proceeding to experimental deployment, the proposed controller is tried on a detailed model developed in [10]. The detailed model accounts for stretchy cables, compliant ground, and a more realistic model of the boom. This is a high-DOF model and cannot be used for control design since an optimization process on this model is not computationally tractable. Cable stretch in MABEL's transmission is an important characteristic of the experimental system not captured by the model of Section II.On running motions, there is severe cable stretch in the leg shape transmission, accounting for nearly 75% of motion in the stance knee at peak cable stretch on certain agressive take-offs. The model of Section II-A assumed no cable stretch and the running controller needs to be modified to account for this discrepancy.

Fig. 5. A typical running step for MABEL. Snapshots are at intervals of 100 ms. The snapshots progress temporally from left to right and from top to bottom. A video of the running experiment is available on YouTube [14].

The cable stretch was identified in [10] and appears as an additional compliant element in series with the physical compliance. Since the running controller uses active force control in the stance phase for creating a virtual compliant element in series with the physical compliance, three sources of compliance (physical springs, cable stretch, virtual compliance) occur in series. Thus, the virtual compliance can be modified in a way such that the effective compliance, after taking the cable stretch into account, has the stiffness that was initially designed for in the absence of cable stretch.

With this modification, the running controller induced stable running at an average speed of 1.95 m/s, and a peak speed of 3.06 m/s. Running speed is measured with respect to the center point of the hip between the two legs. A video of the experiment is available on YouTube [14]. 113 running steps were obtained and the experiment terminated when the power to the robot was cut off. At 2 m/s, the average stance and flight times of 233 ms and 126 ms are obtained, respectively, corresponding to a flight phase that is 35% of the gait. At 3 m/s, the average stance and flight times of 195 ms and 123 ms are obtained respectively, corresponding to a flight phase that is 39% of the gait. An estimated ground clearance of $7.5-10$ cm is obtained. Figure 5 depicts snapshots at 100 ms intervals of a typical running step. Figures 6 and 7 depict the joint angles and motor torques

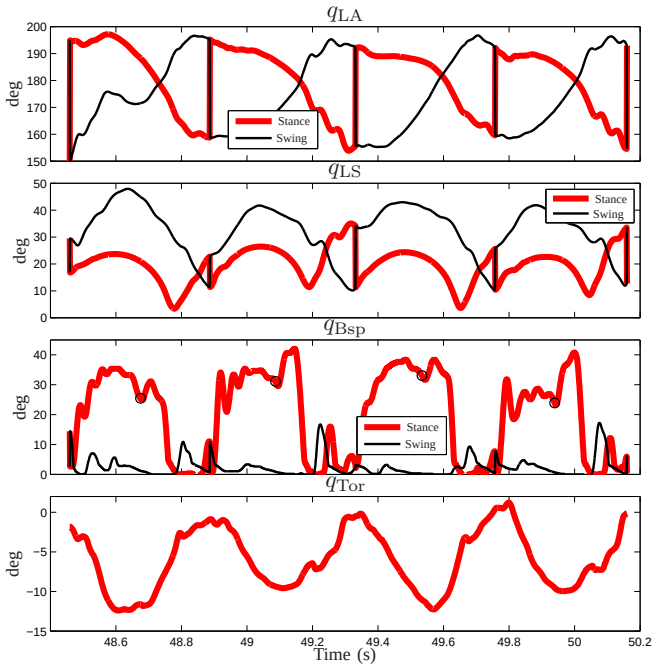

Fig. 6. Experimental plots of joint angles of the stance and swing legs for 4 consecutive steps of running. The circles in the spring plot indicate the location of stance-compression to stance-decompression transitions.

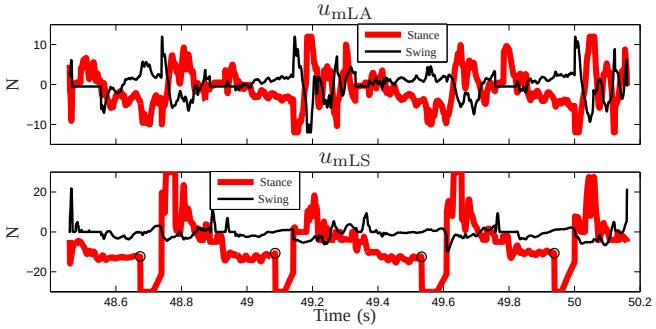

Fig. 7. Experimental plots of motor torques for the stance and swing legs for 4 consecutive steps of running. The circles indicate the location of stance-compression to stance-decompression transitions.

for the stance and swing legs for 4 consecutive steps of the running experiment. The circles in the spring and motor torque plots indicate the location of stance-compression to stance-decompression transitions.

V. Conclusion

A control design based on virtual constraints and the framework of hybrid zero dynamics has been presented to create a compliant and actuated hybrid zero dynamics. An active force control strategy has been implemented within the compliant hybrid zero dynamics. Discrete-event-based control has been employed to create hybrid invariance, exponentially stabilize the periodic gait, and increase the robustness to perturbations in the knee angle at impact and to imperfections in the ground contact model. The resulting controller has been successfully validated in experiments on MABEL achieving running at an average speed of 1.95 m/s, and a peak speed of 3.06 m/s.

Acknowledgment

A. Ramezani assisted with the experiments. Jonathan Hurst designed MABEL. B. Morris, I. Poulakakis, J. Konscol and G. Buche provided a wide range of contributions to this project.

References

[1] B.-K. Cho, S.-S. Park, and J. ho Oh, "Controllers for running in the humanoid robot, HUBO," in *IEEE-RAS International Conference on Humanoid Robots*, Paris, France, December 2009, pp. 385–390.

[2] Y. Hürmüzlü and T. Chang, "Rigid body collisions of a special class of planar kinematic chains," *IEEE Transactions on Systems, Man and Cybernetics*, vol. 22, no. 5, pp. 964–71, 1992.

[3] J. W. Hurst, "The role and implementation of compliance in legged locomotion," Ph.D. dissertation, Carnegie Mellon University, 2008.

[4] S. Kajita, K. Kaneko, and M. Morisawa, "Zmp-based biped running enhanced by toe springs," in *IEEE International Conference on Robotics and Automation*, Roma, Italy, April 2007, pp. 3963–3969.

[5] S. Kajita, T. Nagasaki, K. Kaneko, K. Yokoi, and K. Tanie, "A running controller of humanoid biped hrp-2lr," in *IEEE International Conference on Robotics and Automation*, Barcelona, Spain, April 2005, pp. 616–622.

[6] J. C. Koechling, "The limits of running speed: Experiments with a legged robot," Ph.D. dissertation, Carnegie Mellon University, Pittsburgh, PA, July 1989.

[7] B. J. Morris and J. W. Grizzle, "Hybrid invariant manifolds in systems with impulse effects with application to periodic locomotion in bipedal robots," *IEEE Transactions on Automatic Control*, vol. 54, no. 8, pp. 1751 – 1764, August 2009.

[8] B. J. Morris, E. R. Westervelt, C. Chevallereau, G. Buche, and J. W. Grizzle, *Achieving Bipedal Running with RABBIT: Six Steps Toward Infinity*, ser. Lecture Notes in Control and Information Sciences. Springer Berlin / Heidelberg, 2006, vol. 340, pp. 277–297.

[9] K. Nagasaka, Y. Kuroki, S. Itoh, and J. Yamaguchci, "Integrated motion control for walking, jumping and running on a small bipedal entertainment robot," in *IEEE International Conference on Robotics and Automation*, New Orleans, LA, April 2004, pp. 3189–3194.

[10] H.-W. Park, K. Sreenath, J. W. Hurst, and J. W. Grizzle, "Identification of a bipedal robot with a compliant drivetrain: Parameter estimation for control design," *Control Systems Magazine*, vol. 31, no. 2, pp. 63–88, April 2011.

[11] I. Poulakakis and J. W. Grizzle, "Modeling and control of the monopedal robot thumper," in *IEEE International Conference on Robotics and Automation*, Kobe, Japan, May 12-17 2009, pp. 3327–3334.

[12] ——, "The spring loaded inverted pendulum as the hybrid zero dynamics of an asymmetric hopper," *IEEE Transactions on Automatic Control*, vol. 54, no. 8, pp. 1779–1793, August 2009.

[13] M. H. Raibert, *Legged Robots that Balance*. Cambridge, MA: MIT Press, 1986.

[14] K. Sreenath, H.-W. Park, and J. W. Grizzle. (2011, July) MABEL runs free! [Online]. Available: http://youtu.be/xlOwk6_xpWo

[15] ——, "Embedding active force control within the compliant hybrid zero dynamics to achieve stable, fast running on MABEL," *The International Journal of Robotics Research*, 2011, to be submitted.

[16] K. Sreenath, H.-W. Park, I. Poulakakis, and J. W. Grizzle, "Compliant hybrid zero dynamics controller for achieving stable, efficient and fast bipedal walking on MABEL," *International Journal of Robotics Research*, vol. 30, no. 9, pp. 1170–1193, August 2011.

[17] R. Tajima, D. Honda, and K. Suga, "Fast running experiments involving a humanoid robot," in *IEEE International Conference on Robotics and Automation*, Kobe, Japan, May 2009, pp. 1571–1576.

[18] E. R. Westervelt, J. W. Grizzle, C. Chevallereau, J. H. Choi, and B. Morris, *Feedback Control of Dynamic Bipedal Robot Locomotion*. Boca Raton, FL: Taylor & Francis/CRC Press, 2007.